



Reconstruction and Spatiotemporal Analysis of Global Surface Ocean pCO₂ Considering Sea Area Characteristics

Huisheng Wu, Yunlong Ji, Lejie Wang, Xiaoke Liu, Wenliang Zhou, Long Cui, Yang Wang, Min Liu and Zhuang Li

5 College of Oceanography and Space Informatics, China University of Petroleum (East China), Qingdao, Shandong 266580, China;

Correspondence to: Huisheng Wu (wuhuisheng@upc.edu.cn)

Abstract:

10 The partial pressure of carbon dioxide (pCO₂) on the surface of the ocean is crucial for quantifying and evaluating the ocean carbon budget. Insufficient consideration of the effects at the sea area scale makes it difficult to comprehensively evaluate the spatiotemporal distribution characteristics and variation patterns of pCO₂. This study constructed a pCO₂ evaluation dataset based on LDEO measurement data and multi-source data. After conducting correlation testing on a global, far sea, and near sea scale, a ocean surface pCO₂ evaluation model was
15 constructed using multiple linear regression, convolutional neural network, gated recurrent unit, long short-term memory network, generalized additive model, extreme gradient boosting, least squares boosting, and random forest. Performance evaluation indicates that the random-forest model consistently achieves the best accuracy across all spatial scales, yielding a global RMSE of 6.123 μatm and an R² of 0.986. In the open ocean, RMSE decreases to 4.699 μatm and R² rises to 0.988, whereas in coastal waters RMSE increases to 8.044 μatm and R²
20 declines to 0.972. Based on this, the annual sea surface pCO₂ distribution of 0.25°× 0.25° from 2000 to 2019 was reconstructed. The reconstructed field shows a typical equatorial high/polar low pattern, as well as an overall upward trend consistent with independent observations, with acceleration particularly evident in specific regions of subtropical coastal oceans.

Keywords:

25 Surface ocean pCO₂; Global Oceans; Machine learning; Spatiotemporal changes; Random forest

Synopsis:

This study reconstructs global ocean surface pCO₂ (2000–2019) using multi-source data and machine learning, identifying RF as the optimal model and revealing equatorial-high/polar-low patterns with rising trends.

1. Introduction

30 The partial pressure of carbon dioxide on the surface of the ocean (pCO₂) is an important indicator for measuring the exchange of CO₂ between the ocean and the atmosphere, and can evaluate the contribution of the ocean's carbon absorption and storage capacity to the global carbon cycle (Falkowski et al., 2000; Jain, 2022).

Numerous scholars have conducted research on pCO₂ estimation and distribution reconstruction by combining satellite remote sensing data and machine learning algorithms. In the study of sea surface pCO₂ in local sea areas,

35 Telszewski et al. reconstructed the distribution of pCO₂ in the North Atlantic using self-organizing neural



networks(Qiu et al., 2022); Landschützer et al. reconstructed the distribution map of Atlantic sea surface pCO₂ using self-organizing map feedforward neural network method (Landschützer et al., 2013). Chierici et al. evaluated the feasibility of jointly estimating sea surface pCO₂ in Antarctica and the Pacific region using ship borne measured data and remote sensing data (Chierici et al., 2011). Nakaoka et al. established a nonlinear relationship between sea surface pCO₂ and multiple parameters based on self-organizing neural networks, and reconstructed the spatiotemporal variation of sea surface pCO₂ in the North Pacific (Nakaoka et al., 2013). Marrec et al. used multiple linear regression to estimate the sea surface pCO₂ in the waters of the Northwest European continental shelf (Wang et al., 2021). Gregor et al. proposed methods such as support vector regression and random forest regression to reconstruct the Southern Ocean surface pCO₂ (Gregor et al., 2017); Wang et al. reconstructed the distribution of pCO₂ on the surface of the Southern Ocean using correlation analysis and feed forward neural networks (Marrec et al., 2015). Lohrenz et al. reconstructed the sea surface pCO₂ in the northern Gulf of Mexico using regression tree algorithm (Lohrenz et al., 2021); Chen et al. compared the performance of various methods in estimating surface pCO₂ in the Gulf of Mexico (Chen et al., 2019); Fu et al. applied cubist models to estimate pCO₂ on the surface of the Gulf of Mexico (Fu et al., 2020). Zhang et al. constructed a sea surface pCO₂ regression model for the Baltic Sea region (Zhang et al., 2021). In the study of global ocean surface pCO₂, Landschützer et al. expanded the research scope to the global level, reconstructed the pCO₂ distribution map from 1998 to 2011, and further extended it to 1982 to 2011 (Landschützer et al., 2014; Landschützer et al., 2016). Gregor et al. reconstructed the pCO₂ distribution using various nonlinear regression methods (Gregor et al., 2019). Zhong et al. used generalized regression neural network and stepwise regression algorithm to construct the pCO₂ distribution map (Guorong et al., 2020), and combined stepwise regression algorithm and feed forward neural network, constructed a 1°×1°pCO₂ distribution map from 1992 to 2019 according to the 11 biogeochemical provinces defined by the self-organizing map method (Zhong et al., 2020).

The aim of this study is to construct a multi-regional scale analysis framework for the global ocean, far sea areas, near sea areas, revealing the spatiotemporal variation patterns and driving mechanisms of pCO₂, and providing scientific support for global ocean carbon sink assessment and climate change response.

2. Methodology

2.1 Research Area

The global ocean, excluding the perennial ice-covered waters in the core area of the Arctic Ocean and the permanently frozen areas around the Antarctic continent, has a total area of 336 million square kilometers, accounting for approximately 92.8% of the global ocean surface area. This research focuses on the 0–10-meter water layer in the ocean surface, which is a critical interface for air sea exchange. Due to the complex types of water bodies, sea surface pCO₂ is influenced by various factors. The global ocean was divided into research area scales based on water depth, identifying the areas beyond the continental shelf (water depth>200 meters) as far sea areas and the areas within the range (water depth≤200 meters) as near sea areas.

2.2 Data sources

2.2.1 Actual measurement data

The measured data of pCO₂ is sourced from Global Surface pCO₂ (LDEO) Database V2019 (OCADS - Global Surface pCO₂ (LDEO) Database (noaa.gov)). This dataset covers 14.2 million measured data from 1957 to 2019 using the equalizer CO₂ analyzer system in the global ocean. The dataset provides various types of sea surface pCO₂ measured data. This study selected ocean surface pCO₂ values measured at actual temperatures from 2000 to 2019, which can truly reflect the pCO₂ level at the time of measurement.



2.2.2 Other data

A total of 25 potential influencing factors were selected for the study (Table 1), and their abbreviations are used for convenience. These data are divided into three types of sources: in-situ observations, satellite observations, and numerical models, with good spatiotemporal resolution and coverage, providing reliable data sources for research.

Table 1. Specific information about influencing factors (sort based on its resolution and name)

Variable name	Abbreviation	Spatial resolution	Temporal resolution	Data type	DOI
Mass concentration of chlorophyll a in sea water	chl	0.036	Daily	Satellite observations	https://doi.org/10.48670/moi-00281
Volume attenuation coefficient of downwelling radiative flux in sea water	kd490	0.036	Daily	Satellite observations	https://doi.org/10.48670/moi-00281
Ocean mixed layer thickness defined by sigma theta	mlotst*	0.083	Daily	Numerical models	https://doi.org/10.48670/moi-00021
Sea water salinity	so	0.083	Daily	Numerical models	https://doi.org/10.48670/moi-00021
Sea water potential temperature	thetao	0.083	Daily	Numerical models	https://doi.org/10.48670/moi-00021
Eastward sea water velocity	uo	0.083	Daily	Numerical models	https://doi.org/10.48670/moi-00021
Northward sea water velocity	vo	0.083	Daily	Numerical models	https://doi.org/10.48670/moi-00021
Sea surface height above geoid	zos	0.083	Daily	Numerical models	https://doi.org/10.48670/moi-00021
Sea surface density	dos	0.125	Daily	In-situ observations Satellite observations	https://doi.org/10.48670/moi-00051
Sea surface salinity	sos	0.125	Daily	In-situ observations Satellite observations	https://doi.org/10.48670/moi-00051
Mole concentration of nitrate in sea water	no ₃	0.25	Daily	Numerical models	https://doi.org/10.48670/moi-00019
Mole concentration of dissolved molecular oxygen in sea water	o ₂	0.25	Daily	Numerical models	https://doi.org/10.48670/moi-00019
Mole concentration of phosphate in sea water	po ₄	0.25	Daily	Numerical models	https://doi.org/10.48670/moi-00019
Mole concentration of silicate in sea water	si	0.25	Daily	Numerical models	https://doi.org/10.48670/moi-00019
Surface geostrophic eastward sea	ugos	0.25	Daily	Numerical	https://doi.org/10.48670/mds-003



water velocity				models	27
				In-situ	
				observations	
				Satellite	
				observations	
				Numerical	
				models	
Surface geostrophic northward	vgos	0.25	Daily	In-situ	https://doi.org/10.48670/mds-003
sea water velocity				observations	27
				Satellite	
				observations	
				In-situ	
Ocean mixed layer thickness	mlotst	0.25	Weekly	observations	https://doi.org/10.48670/moi-000
				Satellite	52
				observations	
				In-situ	
Sea water temperature	to	0.25	Weekly	observations	https://doi.org/10.48670/moi-000
				Satellite	52
				observations	
				Satellite	https://doi.org/10.48670/moi-001
Eastward wind	uwind	0.25	Monthly	observations	81
				Satellite	https://doi.org/10.48670/moi-001
Northward wind	vwind	0.25	Monthly	observations	81
				In-situ	https://doi.org/10.48670/moi-000
Aragonite saturation state in sea	ar	1	Monthly	observations	47
water				In-situ	https://doi.org/10.48670/moi-000
Calcite saturation state in sea	ca	1	Monthly	observations	47
water				In-situ	https://doi.org/10.48670/moi-000
Sea water ph reported on total	ph	1	Monthly	observations	47
scale				In-situ	https://doi.org/10.48670/moi-000
Total alkalinity in sea water	talk	1	Monthly	observations	47
				In-situ	https://doi.org/10.48670/moi-000
Dissolved inorganic carbon in sea	tco ₂	1	Monthly	observations	47
water					

2.3 Data Processing

2.3.1 Data Matching

85 To reduce the impact of spatial and temporal resolution differences in multi-source data, we adopted a dual matching strategy to process pCO₂ measured data and potential influencing factors. In the temporal dimension, influencing variables were first aligned with the in-situ pCO₂ observations; temporal gaps were subsequently

90 infilled via nearest-time interpolation to ensure chronological consistency. In the spatial dimension, data points were aligned through precise geographic coordinate matching algorithms, and nearest neighbor interpolation was used to supplement missing points to improve spatial accuracy. After matching, each point contains the measured value of pCO₂, environmental variables, and corresponding spatiotemporal information (year, month, lat, lon).

2.3.2 Analysis of Outliers



The study conducted quality control on the matched data by removing missing values generated during the matching process. According to data statistics and previous research experience (19), measured data below 200 μ atm and above 600 μ atm are classified as outliers. The spatial distribution of outliers is mainly concentrated in coastal areas, reflecting the variability of land sea interaction effects. Outliers are valuable sample data for the study of pCO₂. Through comparative analysis of each route, it was found that many outliers matched the route, and it was determined that their outliers were caused by environmental changes rather than measurement errors. Therefore, valid outliers were retained and only obvious measurement error data were removed. For other environmental variable values, abnormal data was identified and removed based on the 3 σ criterion ($\mu \pm 3\sigma$).

2.3.3 Data Balancing

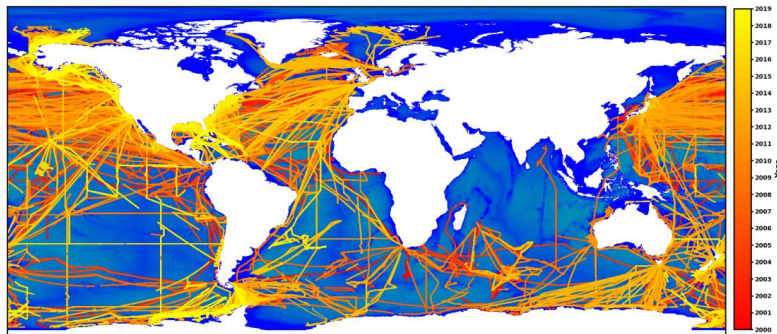
The processed global ocean data was divided into far sea and near sea datasets (Figure 1a, b, c). Statistical analysis shows that the spatial and temporal distribution of data is uneven. Therefore, a 0.25° × 0.25° grid was used for spatial binning, and time binning was performed monthly to construct a spatiotemporal joint binning unit. The granularity setting of this box not only meets the research accuracy requirements, but also maintains compatibility with the spatiotemporal resolution of multi-source data.

Take the arithmetic mean of the data within each unit as the representative value, with the spatial position represented by the grid center point, and the time calculated as the weighted average based on the distribution of data points (Formula 1). This method effectively balances the data distribution while ensuring accuracy.

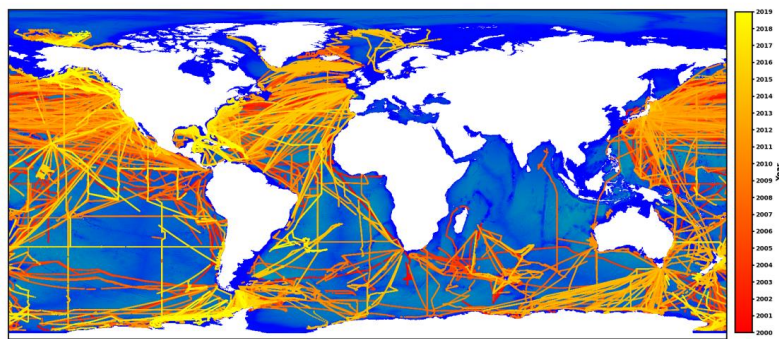
$$t_{avg} = \frac{\sum_{i=1}^n w_i t_i}{\sum_{i=1}^n w_i} \quad (1)$$

$$w_i = \Delta t_i \quad (2)$$

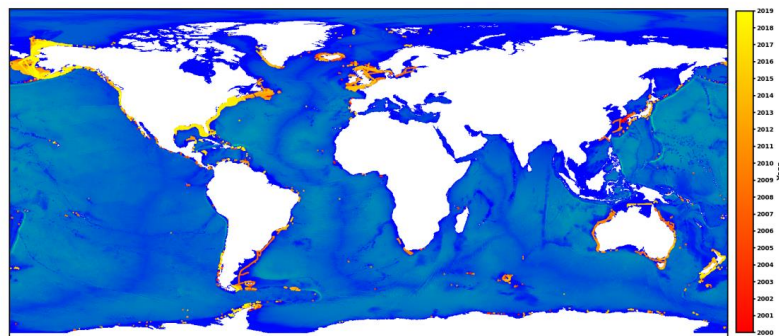
In the formula, t_{avg} is the weighted average time of the spatiotemporal box, n is the total amount of data in the spatiotemporal box, w_i is the weight of the i -th data point, t_i is the time of the i -th data point, and Δt_i is the sampling time interval between the i -th data point and the previous point. After data balancing processing, the dataset for this study was finally constructed, laying a solid data foundation for the construction of multi-scale models.



(a)



(b)



(c)

Figure 1. The spatiotemporal distribution of datasets at different scales.(a)Global spatial distribution of ocean data.(b)Spatial distribution of data in far sea areas.(c)Spatial distribution of data in near sea areas.

115 2.4 Spearman correlation analysis of pCO₂ drivers

The potential influencing factors involved do not fully follow a normal distribution, and there is a non-linear relationship between pCO₂. Therefore, selecting appropriate correlation indicators is particularly crucial. The Spearman correlation coefficient can effectively reveal the correlation between data (Formula 3).

$$\rho = 1 - \frac{\sum_{i=1}^n D_i^2}{n(n^2-1)} \quad (3)$$

120 In the formula, ρ represents the correlation coefficient, d represents the level difference of the variable, and n represents the sample size of the variable. The range of values for ρ is between -1 and 1, where -1 indicates a complete negative correlation between the influencing factors and pCO₂, 1 indicates a complete positive correlation, and 0 indicates no correlation.

2.5 Model selection



125 To evaluate the modeling ability of different algorithms for pCO₂, we constructed eight comparative models at
different research regions, including multiple linear regression (MLR), convolutional neural network (CNN),
gated recurrent unit (GRU), long short term memory (LSTM), generalized additive models (GAM), extreme
gradient boosting (XGBoost), least squares boosting (LSBoost), and random forest (RF). MLR serves as a
130 baseline that linearly links temperature, salinity and nutrients to sea-surface pCO₂. CNN extracts spatial features
via convolution and pooling layers to produce fine-scale pCO₂ distributions, while GRU and LSTM, with their
update-reset gates and memory cells, capture long-term temporal dependencies of oceanic periodic changes on
pCO₂ for historical-to-future prediction. GAM relaxes the linearity assumption by modeling each predictor's
additive nonlinear effect on pCO₂. XGBoost and LSBoost iteratively optimize tree ensembles through gradient
boosting or weighted residuals to uncover complex nonlinear relationships between high-dimensional features
135 and pCO₂. Finally, RF constructs and averages many decision trees on random feature subsets, delivering robust
pCO₂ estimates for large-scale ocean datasets.

2.6 Performance evaluation

The datasets at different research regions were randomly divided into training, validation, and testing sets in an
8:1:1 ratio. Five statistical methods, Mean Absolute Error (MAE, μatm) – the average absolute difference
140 between predicted and in-situ pCO₂, indicating overall bias; Mean Absolute Percentage Error (MAPE, %)-the
relative error scaled by the observed pCO₂, enabling comparison across regions with contrasting background
concentrations; Mean Squared Error (MSE, μatm^2) – the squared deviations averaged over all samples,
emphasizing larger pCO₂ discrepancies; Root Mean Squared Error (RMSE, μatm) – the square root of MSE,
providing a metric in the original pCO₂ units that is sensitive to outliers; Coefficient of Determination (R²) – the
145 proportion of pCO₂ variance explained by the model, with values approaching unity signifying high predictive
skill.

$$\text{MAE} = \frac{1}{n} \sum_{i=1}^n |\hat{y}_i - y_i| \quad (4)$$

$$\text{MAPE} = \frac{100\%}{n} \sum_{i=1}^n \left| \frac{\hat{y}_i - y_i}{y_i} \right| \quad (5)$$

$$\text{MSE} = \frac{1}{n} \sum_{i=1}^n (\hat{y}_i - y_i)^2 \quad (6)$$

$$\text{RMSE} = \sqrt{\frac{1}{n} \sum_{i=1}^n (\hat{y}_i - y_i)^2} \quad (7)$$

$$R^2 = 1 - \frac{\sum_{i=1}^n (y_i - \bar{y})^2}{\sum_{i=1}^n (y_i - \hat{y}_i)^2} \quad (8)$$

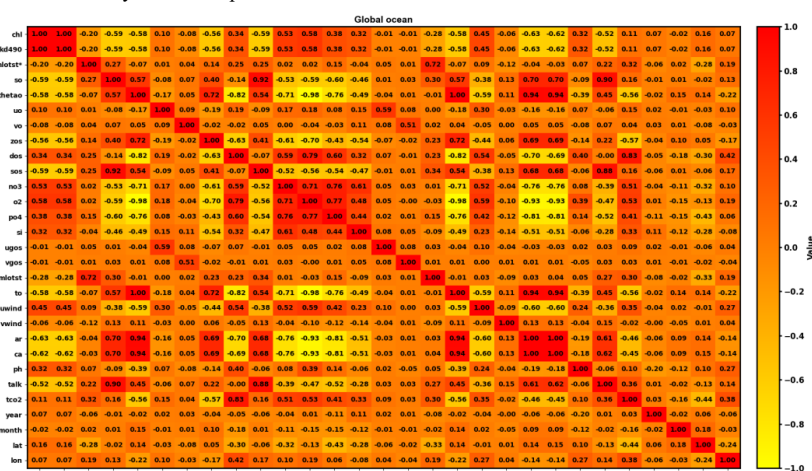
In the formula, n is the number of pCO₂ observations; y_i denotes the in-situ measured pCO₂ (μatm) for the i -th
sample, \hat{y}_i is the corresponding model-estimated pCO₂, \bar{y} represents the mean of all measured pCO₂ values.

3. Results and discussion

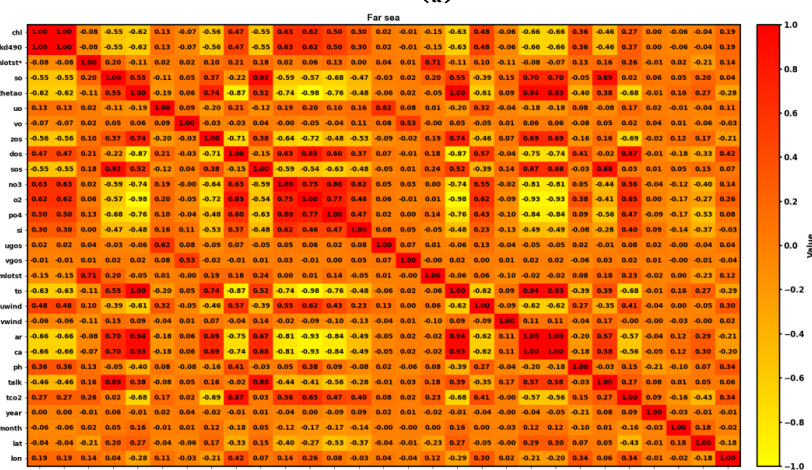
3.1 Correlation detection

3.1.1 Interaction detection

Interactive detection of variables was conducted in global oceans, far sea areas, and near sea areas (Figure 2). The
concentration of chlorophyll and the volume attenuation coefficient of downwelling radiative flux have a p-value
of 1 at all research area scales, indicating collinearity in numerical values. However, they respectively reflect



1. -0.15 -4



(b)

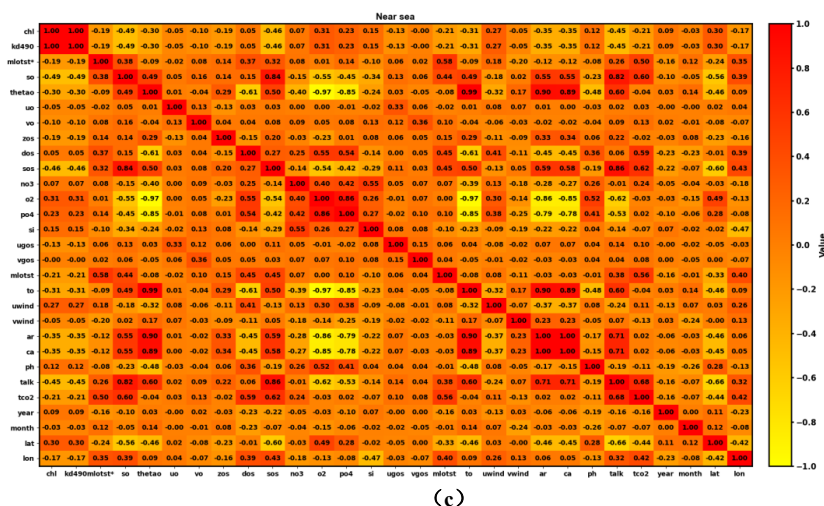


Figure 2. Results of interaction detection between variables at different research area scales. (a) Global Ocean Interaction Detection Results. (b) Interaction detection results in far sea areas. (c) Interactive detection results in near sea areas.

3.1.2 Single factor detection

The correlation between surface pCO₂ and various influencing factors (Figure 3) was analyzed. The results indicate that at different regional scales, there is a significant negative correlation between pCO₂ and ph, meaning that the stronger the acidity of seawater, the higher the surface pCO₂; the stronger the alkalinity, the lower the surface pCO₂. At the same time, surface pCO₂ is significantly positively correlated with temperature. In far sea areas, the negative correlation between pCO₂ and chlorophyll concentration and diffuse reflectance attenuation coefficient is more significant, indicating that it has higher stability and balance in regulating pCO₂. In contrast, the above correlation in near sea areas is weaker due to land-based pollution, human activities, and environmental changes, but the negative correlation between pCO₂ and seawater acidity is stronger. When selecting variables, the study included factors with a p-value greater than 0.1 or less than -0.1 in the screening range to ensure the validity of the results and improve model performance (Table 2). Additionally, SHAP method was used to quantitatively evaluate the contributions of various influencing factors to surface pCO₂ (20). There were differences in the contributions of influencing factors at different scales. The ph is the core driving factor at all scales, but its contribution intensity follows a distribution pattern of "far sea areas>global oceans>near sea areas"; The contribution of other factors shows significant regional heterogeneity, such as talk being the second key factor at the global ocean scale, while the contribution rate of o₂ in near sea areas has significantly increased, making ar a region specific factor.

Table 2. Selection results of influencing factors at different area scales

Research scale	Influence factor
Global Ocean	ph, o ₂ , chl, kd490, dos, uwind, po ₄ , lon, zos, month, sos, year, talk, ca, so, ar, to, thetao
Far sea	ph, chl, kd490, o ₂ , dos, lon, uwind, po ₄ , zos, month, sos, talk, so, ca, ar, year, to, thetao
Near sea	ph, o ₂ , po ₄ , lat, dos, no ₃ , chl, kd490, mltot*, tco ₂ , lon, month, ca, ar, sos,

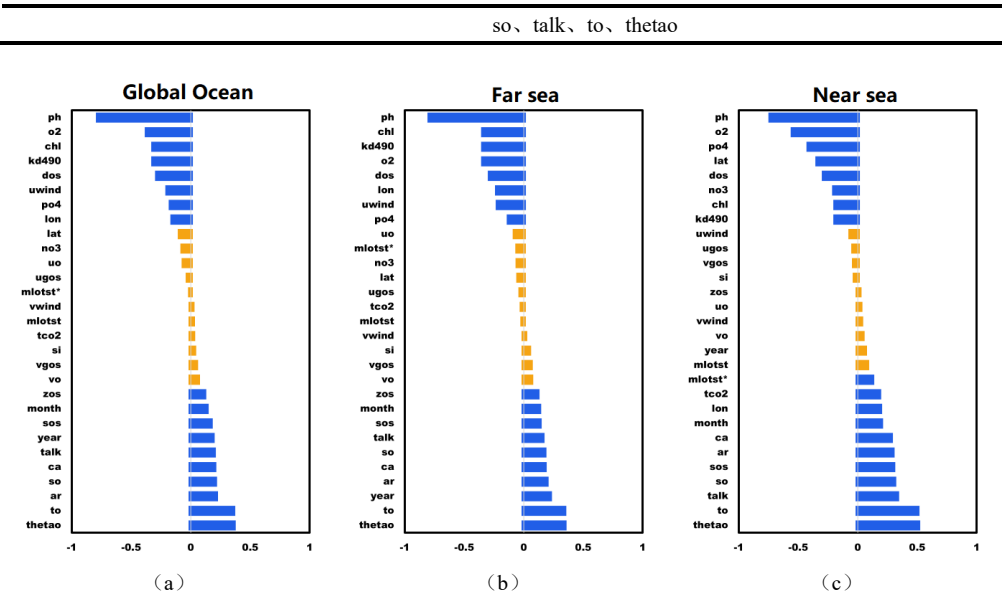


Figure 3. Single factor detection results at different research area scales. (a) Global ocean single factor detection results. (b) Far sea single factor detection results. (c) Near sea single factor detection results

3.2 Model construction and evaluation

3.2.1 Construction and evaluation of global ocean surface pCO₂ model

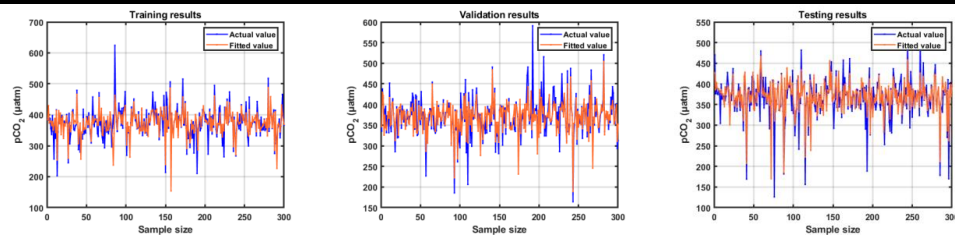
Different models exhibit significant performance differences in evaluating surface pCO₂ at the global ocean scale (Figure 4). Specifically, there is a significant gap between the model values of MLR, CNN, and GRU and the true values, especially in the low value (<300μatm) and high value (>500μatm) ranges where the fitting effect is poor (Table 3). The deviation is due to the model's insufficient ability to capture nonlinear relationships in complex marine environments, limitations in handling extreme values, and the model's own structure is not sufficient to adapt to complex data features. The LSTM and GAM models have relatively large errors and poor performance, indicating deficiencies in capturing the characteristics of surface pCO₂ changes. When extreme fluctuations occur in surface pCO₂, the fitting ability significantly decreases. The comprehensive performance of XGBoost and LSBoost has significantly improved, with MAE reduced to 15μatm~18μatm, RMSE reduced to 25μatm~30μatm, and R² exceeding 0.7. The effective explanation of multivariate nonlinear relationships and the application of model ensemble strategies have improved the accuracy of the two models within the normal range (300μatm~500μatm), but the extreme values processing still needs to be improved. The performance of RF is the best among all models, with MAE reduced to below 4μatm, RMSE reduced to around 6μatm, and R² reaching above 0.9. It not only achieves accurate fitting in the range of 300μatm~500μatm values, but also in the low and high value ranges. The good adaptability of RF to high-dimensional data and a large number of samples makes it perform well in fitting tasks in complex marine environments.

Table 3. Performance parameters of different models in the global ocean

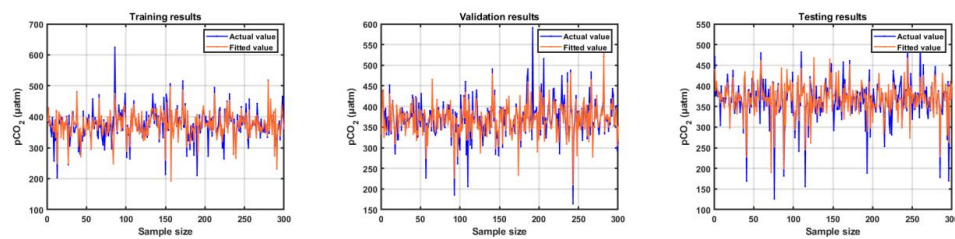
Model		MAE/μatm	MAPE	MSE/μatm ²	RMSE/μatm	R ²
Trainin	RF	3.895	0.011	46.162	6.794	0.983
	LSBoost	15.626	0.045	664.186	25.772	0.783



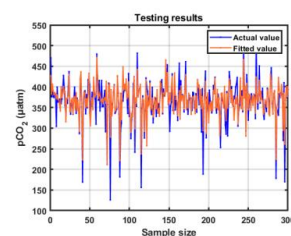
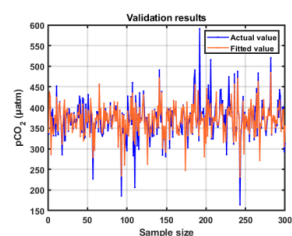
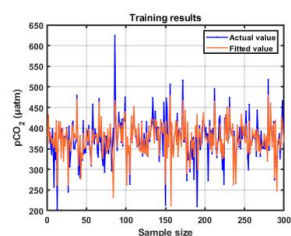
	XGBoost	17.262	0.051	908.879	30.148	0.703
	GAM	19.903	0.058	1398.695	37.399	0.543
	LSTM	18.664	0.055	1430.072	37.816	0.533
	GRU	19.053	0.056	1480.157	38.473	0.516
	CNN	19.903	0.058	1484.621	38.531	0.515
	MLR	19.952	0.058	1615.155	40.189	0.472
Validation	RF	3.902	0.011	46.099	6.790	0.983
	LSBoost	15.604	0.045	661.203	25.714	0.788
	XGBoost	17.255	0.051	910.387	30.173	0.708
	GAM	19.905	0.058	1429.372	37.807	0.541
	LSTM	18.675	0.055	1463.378	38.254	0.529
	GRU	19.059	0.056	1515.286	38.927	0.513
	CNN	19.901	0.058	1520.882	38.999	0.511
	MLR	19.969	0.058	1656.093	40.695	0.468
Testing	RF	3.697	0.010	37.485	6.123	0.986
	LSBoost	15.602	0.045	660.401	25.698	0.785
	XGBoost	17.284	0.051	914.165	30.235	0.703
	GAM	19.916	0.058	1399.851	37.415	0.545
	LSTM	18.690	0.055	1431.489	37.835	0.535
	GRU	19.079	0.056	1483.044	38.510	0.518
	CNN	19.927	0.058	1488.331	38.579	0.516
	MLR	19.982	0.058	1621.378	40.266	0.473



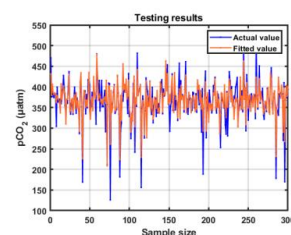
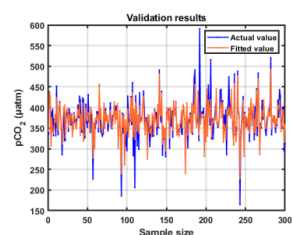
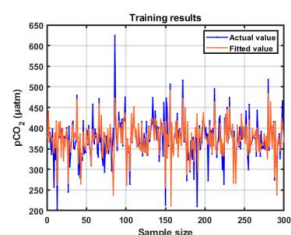
(a) MLR



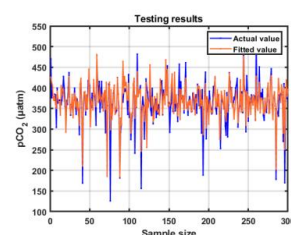
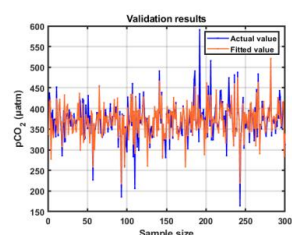
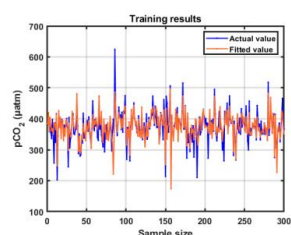
(b) CNN



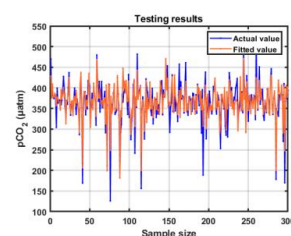
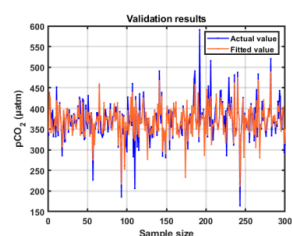
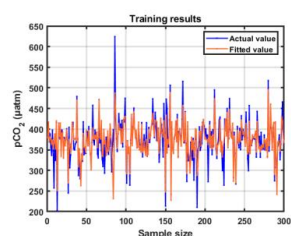
(c) GRU



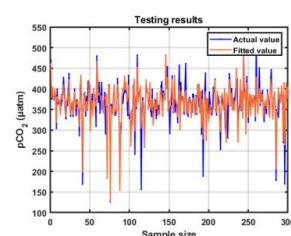
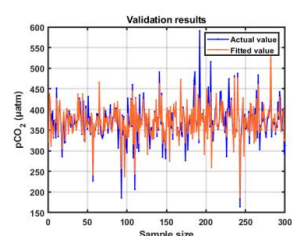
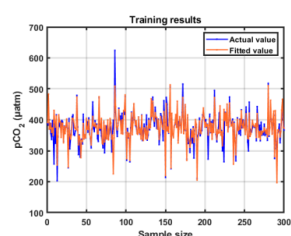
(d) LSTM



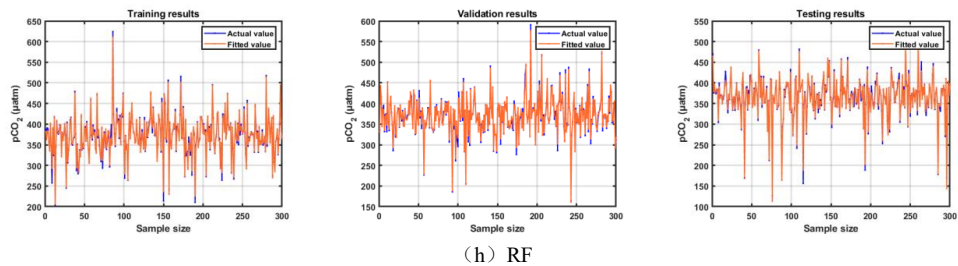
(e) GAM



(f) XGBoost



(g) LSBoost



205 **Figure 4. Model performance at the global ocean**

3.2.2 Construction and evaluation of surface pCO₂ model in far sea areas

The far sea environment is relatively stable, and the model performance has been improved (Table 4). The bias of MLR, CNN, and GRU models has been reduced, with MAE ranging from 14µatm to 15µatm, RMSE above 26µatm, and R² remaining around 0.6. The MAE of LSTM and GAM is around 14µatm; RMSE is above 25µatm, and R² is around 0.64. The performance of the two models has improved compared to extreme value ranges, thanks to the ability of LSTM to process time series data and capture the dynamic characteristics of surface pCO₂ over time, and GAM fitted the relationship between surface pCO₂ and influencing factors by constructing a nonlinear additive model. XGBoost and LSBoost perform even better in far sea areas, especially with high fitting accuracy in the range of 300µatm~500µatm, MAE around 11µatm~13µatm, RMSE reduced to below 23µatm, and R² increased to around 0.8. The model performance of RF in far sea areas is also optimal, relying on strong generalization ability and feature selection mechanisms to effectively address the variability factors in marine environments.

Table 4. Performance parameters of different models in the far sea areas

	Model	MAE/µatm	MAPE	MSE/µatm ²	RMSE/µatm	R ²
Training	RF	3.068	0.009	27.456	5.240	0.985
	LSBoost	11.509	0.033	337.852	18.381	0.813
	XGBoost	13.191	0.038	500.054	22.362	0.723
	GAM	14.066	0.040	623.501	24.970	0.654
	LSTM	14.160	0.041	647.853	25.453	0.641
	GRU	14.377	0.041	665.920	25.805	0.631
	CNN	14.882	0.043	681.120	26.098	0.623
	MLR	15.274	0.044	737.902	27.164	0.591
Validation	RF	3.061	0.009	27.110	5.207	0.985
	LSBoost	11.532	0.032	338.102	18.388	0.814
	XGBoost	13.243	0.038	511.318	22.612	0.719
	GAM	14.143	0.040	644.144	25.380	0.646
	LSTM	14.219	0.040	667.947	25.845	0.632
	GRU	14.441	0.041	686.351	26.198	0.622
	CNN	14.929	0.042	701.278	26.482	0.614
	MLR	15.336	0.043	758.818	27.547	0.582
Testing	RF	2.900	0.008	22.082	4.699	0.988
	LSBoost	11.521	0.032	339.772	18.433	0.813
	XGBoost	13.223	0.038	508.771	22.556	0.720



GAM	14.104	0.040	638.362	25.266	0.649
LSTM	14.201	0.040	663.510	25.759	0.635
GRU	14.423	0.041	681.866	26.113	0.625
CNN	14.914	0.042	696.718	26.395	0.617
MLR	15.316	0.043	754.142	27.462	0.585

220 3.2.3 Construction and evaluation of surface pCO₂ model in near sea areas

Due to various complex factors, the spatiotemporal distribution of surface pCO₂ in the near sea area exhibits high variability, resulting in a decrease in the performance of the model. Table 5 results show that MLR, CNN, and GRU have limitations in handling complex nonlinear relationships. In the low and high value ranges, the MAE of the three models reaches over 34μatm, RMSE reaches over 62μatm, and R² is below 0.5. LSTM constructs a nonlinear additive model through its gating mechanism and GAM, which improves the fitting ability to a certain extent. The MAE of the model is in the range of 33μatm~34μatm; the RMSE is in the range of 56μatm~58μatm, and the R² remains in the range of 0.55~0.60, but there is still deviation in the extreme numerical range. XGBoost and LSBoost improved the accuracy of fitting extreme values by constructing multiple weak learners to combine the fitting results. The MAE of both models decreased to around 23μatm~27μatm, the RMSE remained around 35μatm~42μatm, and the R² increased to the range of 0.75~0.85. RF constructed multiple decision trees and integrated the fitting results to adapt to the variability and variability of the near sea environment, demonstrating robust fitting performance. Its MAE was below 5μatm; RMSE was about 8μatm, and R² remained above 0.95, significantly outperforming other models.

Table 5. Performance parameters of different models in the near sea areas

	Model	MAE/μatm	MAPE	MSE/μatm ²	RMSE/μatm	R ²
Training	RF	5.396	0.016	98.332	9.916	0.977
	LSBoost	23.673	0.071	1267.869	35.607	0.833
	XGBoost	27.298	0.083	1783.422	42.231	0.765
	GAM	34.088	0.102	3058.776	55.306	0.597
	LSTM	32.738	0.100	3273.977	57.219	0.569
	GRU	34.022	0.103	3754.637	61.275	0.505
	CNN	36.309	0.110	3989.599	63.163	0.474
	MLR	36.264	0.109	4426.775	66.534	0.417
Validation	RF	5.346	0.016	93.028	9.645	0.978
	LSBoost	23.604	0.071	1263.495	35.546	0.832
	XGBoost	27.234	0.083	1766.706	42.032	0.765
	GAM	34.040	0.102	3033.228	55.075	0.596
	LSTM	32.686	0.100	3259.080	57.088	0.566
	GRU	33.987	0.103	3727.152	61.050	0.504
	CNN	36.239	0.110	3955.729	62.895	0.474
	MLR	36.188	0.109	4387.955	66.242	0.416
Testing	RF	4.756	0.014	64.708	8.044	0.972
	LSBoost	23.564	0.071	1244.921	35.283	0.839
	XGBoost	27.299	0.083	1788.363	42.289	0.769
	GAM	34.204	0.102	3134.086	55.983	0.595
	LSTM	32.911	0.100	3394.342	58.261	0.562



GRU	34.236	0.103	3904.309	62.485	0.496
CNN	36.465	0.110	4132.316	64.283	0.466
MLR	36.405	0.109	4594.537	67.783	0.406

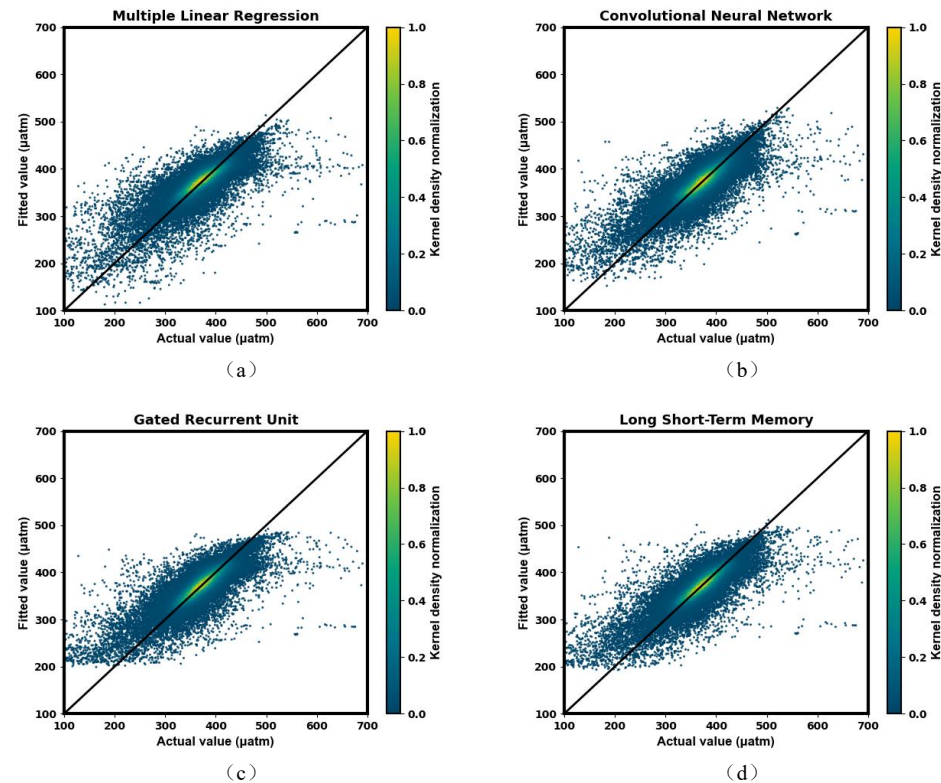
235

3.3 Independent validation of the model

The surface pCO₂ models were independently validated at different regional scales, inputting data independent of the model construction, comparing the accuracy of the fitted values with the true values, and evaluating the applicability and accuracy of the model in complex marine environments. The scatter plot with true values as the x-axis and fitted values as the y-axis was drawn, with colors representing kernel density to reflect the distribution trend of points. At the global ocean scale (Figure 5), the scatter distribution of MLR, CNN, GRU, LSTM, and GAM shows a large elliptical shape, and the fitted values deviate significantly from the true values, especially around the extreme value of pCO₂ on the sea surface. The scatter distributions of XGBoost and LSBoost have shrunk. The RF model has the best fitting performance, with a clear convergence of the scatter distribution, concentrated on Y=X line, and can effectively avoid errors in the extreme value region, indicating that its fitted value is consistent with the true value and has good stability.

240

245



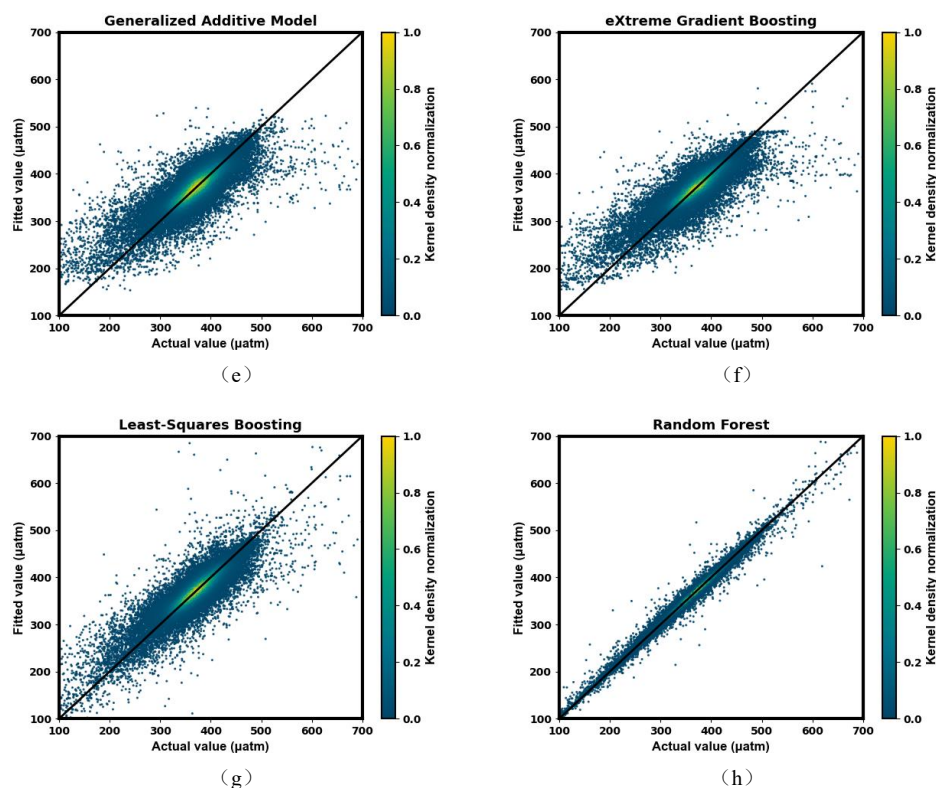
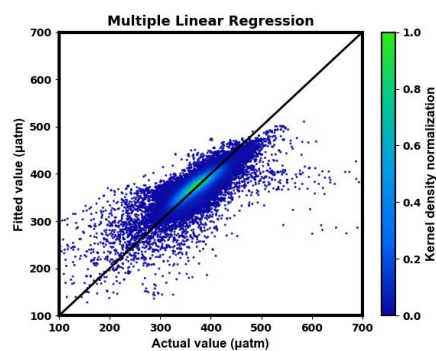


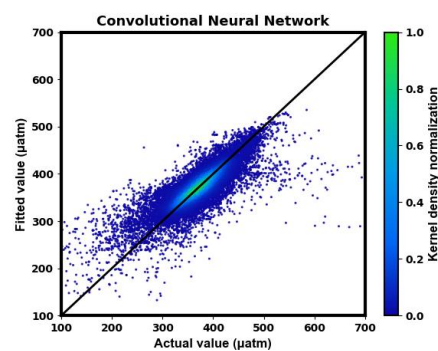
Figure 5. Independent verification performance of the models in the global ocean, right axis: Normalized probability density of model residuals. (a) MLR, (b) CNN, (c) GRU, (d) LSTM, (e) GAM, (f) XGBoost, (g) LSBoost, (h) RF

250 In far sea areas (Figure 6), the scatter points of MLR, CNN, GRU, LSTM, GAM, and XGBoost models exhibit elliptical distribution and diverge at both ends, indicating their limitations in dealing with extreme fluctuations of surface pCO₂. The scatter distribution ellipse of the LSBoost model significantly shrinks, and the divergence situation converges at extreme values, improving the fitting accuracy. The scatter distribution of the RF model is a flat ellipse, with the minimum difference between the fitted value and the true value, effectively reducing extreme errors.

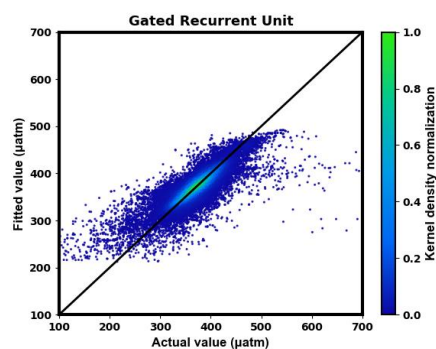
255



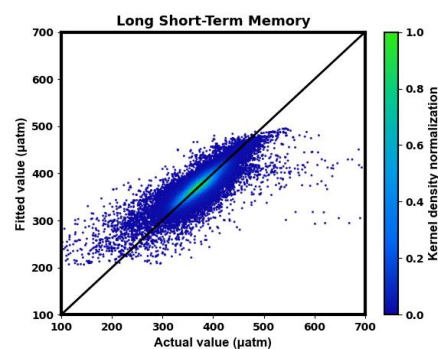
(a)



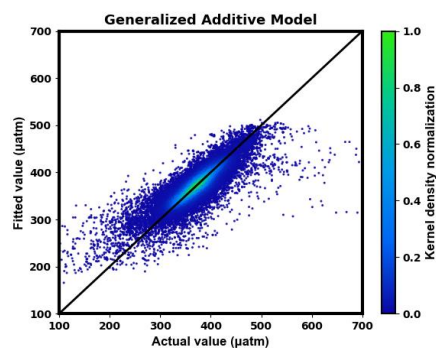
(b)



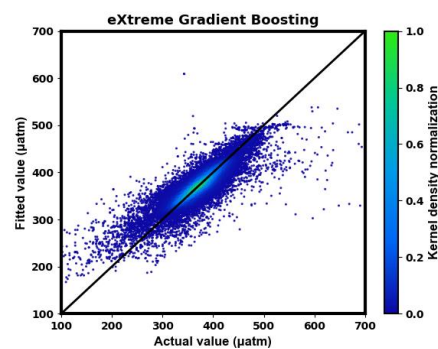
(c)



(d)



(e)



(f)

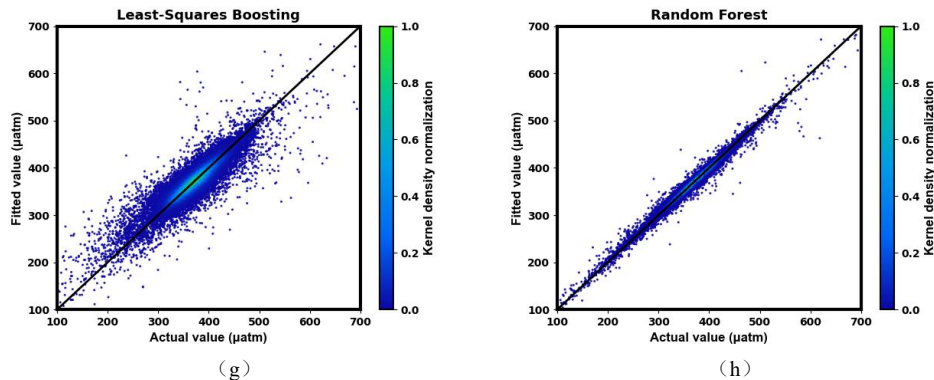
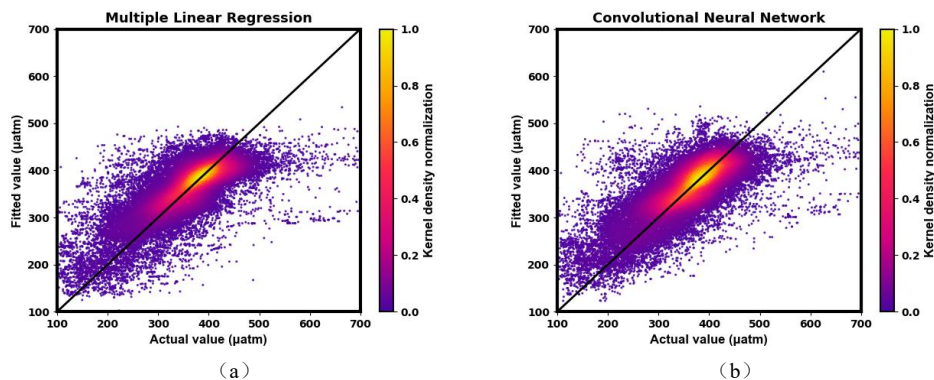


Figure 6. Independent verification performance of the models in the far sea areas, right axis: Normalized probability density of model residuals. (a) MLR, (b) CNN, (c) GRU, (d) LSTM, (e) GAM, (f) XGBoost, (g) LSBoost, (h) RF

In the independent validation of models in near sea areas, each model showed different performances (Figure 7).
The scatter of MLR, CNN, GRU, and LSTM shows an irregular distribution, with significant differences between the fitted values and the true values, and severe divergence in high-value areas. This is due to the high variability in near sea areas, which makes it difficult for the model to cope with. The scatter distribution of GAM and XGBoost has begun to show an elliptical shape, which has certain adaptability to complex environments. The scatter distribution of LSBoost shows a clear elliptical shape, which improves the fitting stability. The RF model shows significant improvement in performance, with overall convergence of scatter distribution and no significant divergence in both low and high value oceans. It can effectively reduce extreme errors and reconstruct surface pCO₂ with high accuracy in complex near sea environments.



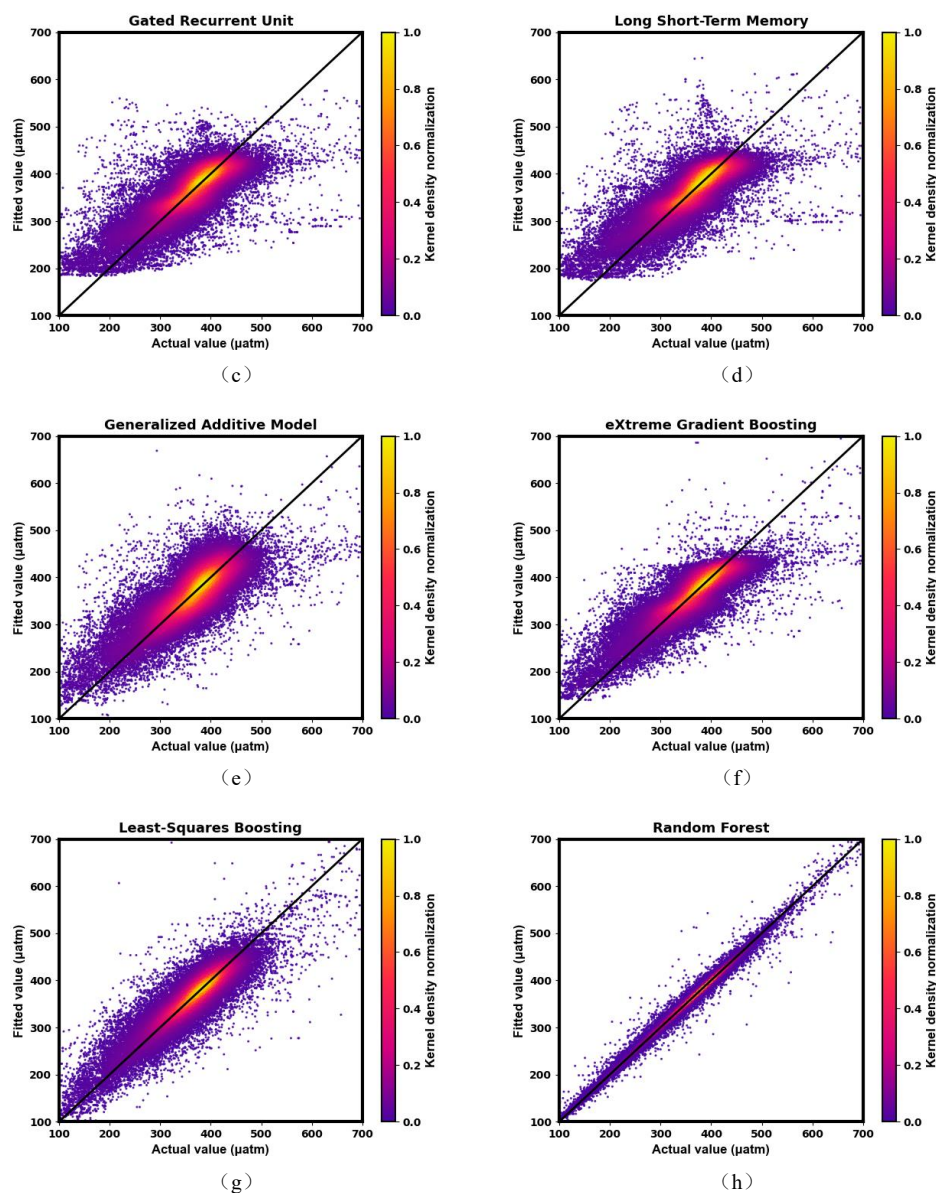


Figure 7. Independent verification performance of the models in the near sea areas, right axis: Normalized probability density of model residuals. (a) MLR, (b) CNN, (c) GRU, (d) LSTM, (e) GAM, (f) XGBoost, (g) LSBoost, (h) RF

3.4 Reconstruction of surface pCO₂

The multi-source data was input into the constructed RF model at different area scales, with extracting the variable values of influencing factors from the multi-source data grid by grid to fit the surface pCO₂ values of the corresponding grid. If there are missing values in a certain grid in the multi-source data, the corresponding surface pCO₂ value at that location will be output as a blank value, ensuring that the reconstructed results are completely



based on the original data. The final generation of the surface $p\text{CO}_2$ distribution map for the year 2000–2019 at $0.25^\circ \times 0.25^\circ$ is based on the original data.

The reconstruction results of surface $p\text{CO}_2$ at the global ocean scale are consistent with the distribution characteristics of LDEO actual observation data, confirming that the RF model can effectively capture the spatial distribution pattern of global ocean surface $p\text{CO}_2$. Through the reconstruction results (Figure 8), it was found that the spatial distribution of surface $p\text{CO}_2$ exhibits a clear latitude dependence, with a distribution pattern of "high at the equator and low at the poles". The independent observation data based on the route was compared with the reconstruction results obtained at the closest collection time. The global ocean surface $p\text{CO}_2$ reconstruction result showed MAE of $11.067 \mu\text{atm}$, MAPE of 0.037, MSE of $396.060 \mu\text{atm}^2$, RMSE of $19.901 \mu\text{atm}$, and R^2 of 0.816. This indicates that the deviation between the reconstructed results and the actual observed data is small, and can accurately reflect the average distribution characteristics of surface $p\text{CO}_2$.

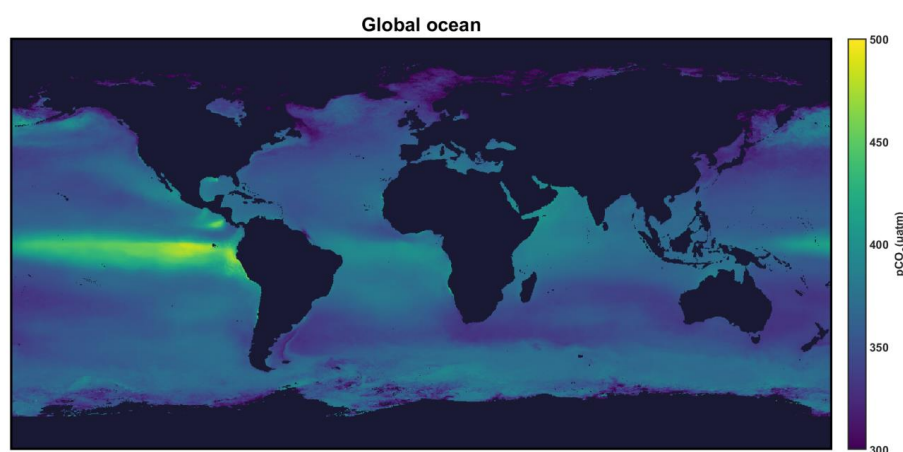


Figure 8. Surface ocean $p\text{CO}_2$ products in the global ocean

Compared with other existing studies on the reconstruction of surface $p\text{CO}_2$, these methods are highly consistent with our results in the reconstructed spatial model pattern (Zhong et al., 2022; Chau et al., 2021; Chau et al., 2022). Although different studies have used different data sources, models, or methods, similar conclusions can be drawn when describing the overall distribution characteristics of $p\text{CO}_2$ on the global ocean surface, which to some extent verifies the reliability and accuracy of the reconstructed results. This study uses high-resolution data and RF models to make the reconstruction results more detailed, especially in the high latitude marginal sea areas of the North and South Poles.

The reconstruction results of the far sea region showed that the surface $p\text{CO}_2$ in the equatorial low latitude region was higher, while the surface $p\text{CO}_2$ in the polar high latitude region was lower (Figure 9). We evaluated the difference in fitting accuracy between the far sea regional model and the global ocean model in the far sea areas, by comparing independent observation data based on flight routes with the reconstructed results of the two models. The results showed that the MAE of the far-sea model was $9.060 \mu\text{atm}$, the MAPE was 0.027, the MSE was $269.511 \mu\text{atm}^2$, the RMSE was $16.417 \mu\text{atm}$, and R^2 was 0.826; the MAE of the global model was $9.125 \mu\text{atm}$, the MAPE was 0.027, the MSE was $275.582 \mu\text{atm}^2$, the RMSE was $16.601 \mu\text{atm}$, and R^2 was 0.822. The reconstruction accuracy of the far sea area model has slightly improved compared to the global ocean model in the far sea area (Figure 10), indicating that the optimization of the far sea area model in local areas has improved the



305 reconstruction accuracy. However, the global ocean model can still provide accurate surface $p\text{CO}_2$ fitting in the far
sea area by adapting to the overall ocean environment.

To verify the accuracy of the time series reconstruction of the model, a comparative analysis was conducted on the
temporal changes between the observation data of the Hawaii Ocean Time series (HOT) and the reconstruction
results of the global ocean and far sea areas (Figure 11). The results showed that the temporal trends of both scales
310 were consistent with the actual measurement data of the Hawaii observation station. Research has shown that the
model performs well in fitting the dynamic changes of time series and can accurately reflect the temporal evolution
of surface $p\text{CO}_2$.

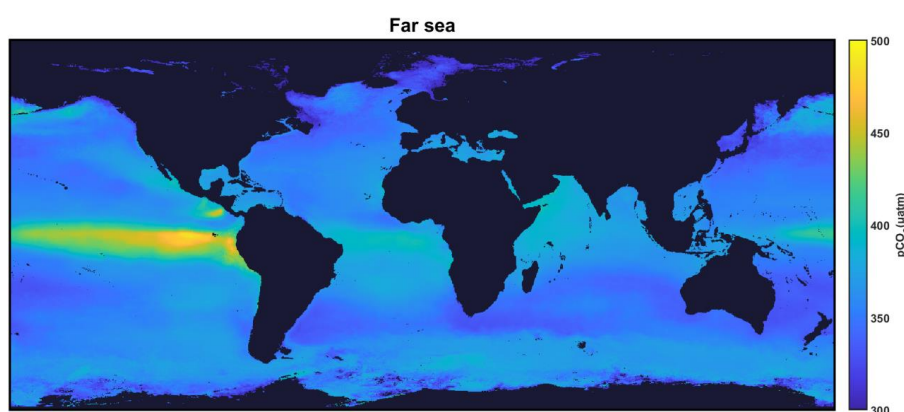
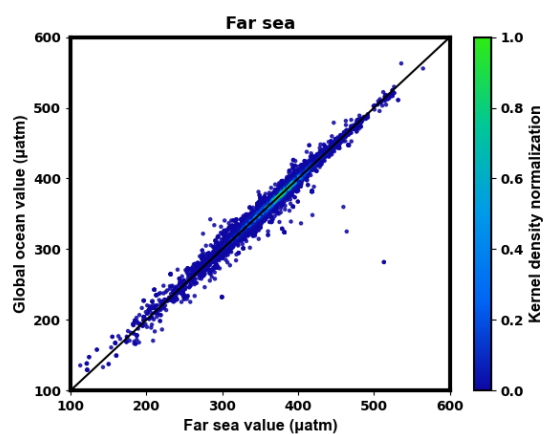


Figure 9. Surface ocean $p\text{CO}_2$ products in the far sea areas



315

Figure 10. Comparison of reconstruction accuracy in the far sea areas using different scale models, right
axis: Normalized probability density of model residuals.

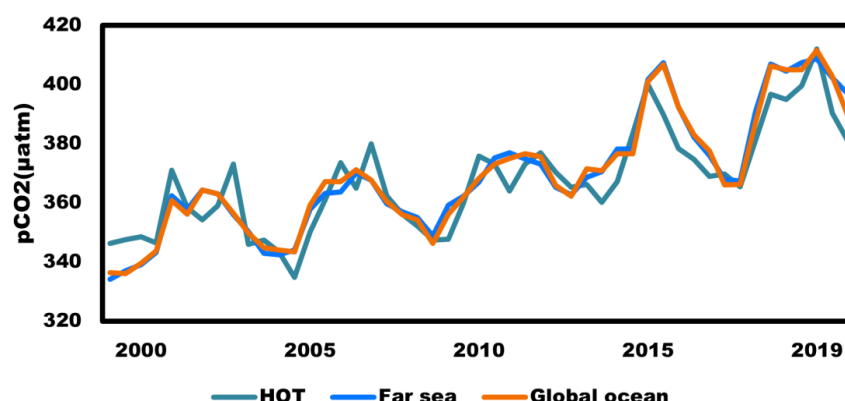


Figure 11. Independent verification based on time-series observation stations

320 The reconstruction results of surface $p\text{CO}_2$ in the near sea area showed (Figure 12) that the surface $p\text{CO}_2$ values in the low latitude near sea areas on both sides of the equator were higher, which was closely related to factors such as high seawater temperature and vigorous evaporation. The seawater temperature in high latitude oceans is lower, causing changes in ocean circulation and mixing processes, and the overall trend of surface $p\text{CO}_2$ is decreasing. A comparison was made between the fitting accuracy of the near sea area model and the global ocean model in the near sea region. The results showed that the MAE of the near-shore model was 20.145 μatm , the MAPE was 0.065, the MSE was 983.726 μatm^2 , the RMSE was 31.364 μatm , and R^2 was 0.797; the MAE of the global model was 20.324 μatm , the MAPE was 0.065, the MSE was 999.147 μatm^2 , the RMSE was 31.609 μatm , and R^2 was 0.794. The reconstruction effect of the near sea area model has been improved compared to the reconstruction results of the global ocean model in the near sea area (Figure 13), indicating that the use of RF can model the complex marine environment in the near sea area and accurately reflect the distribution characteristics of surface $p\text{CO}_2$ in the region.

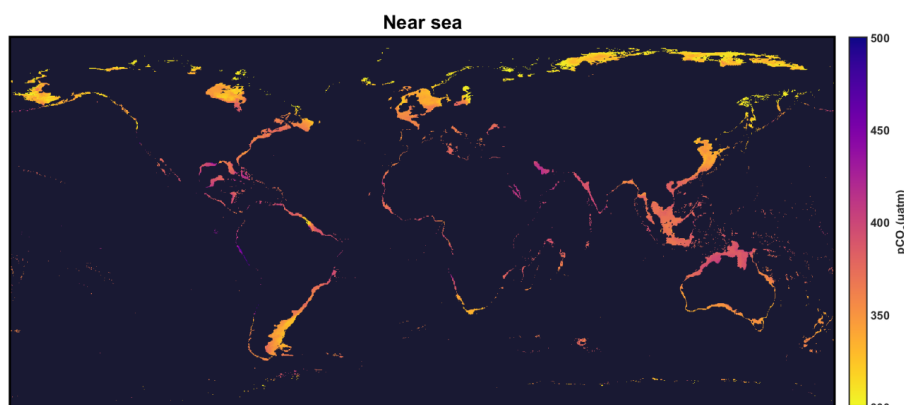
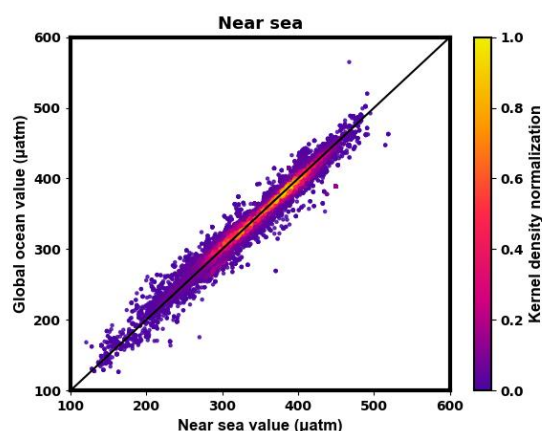


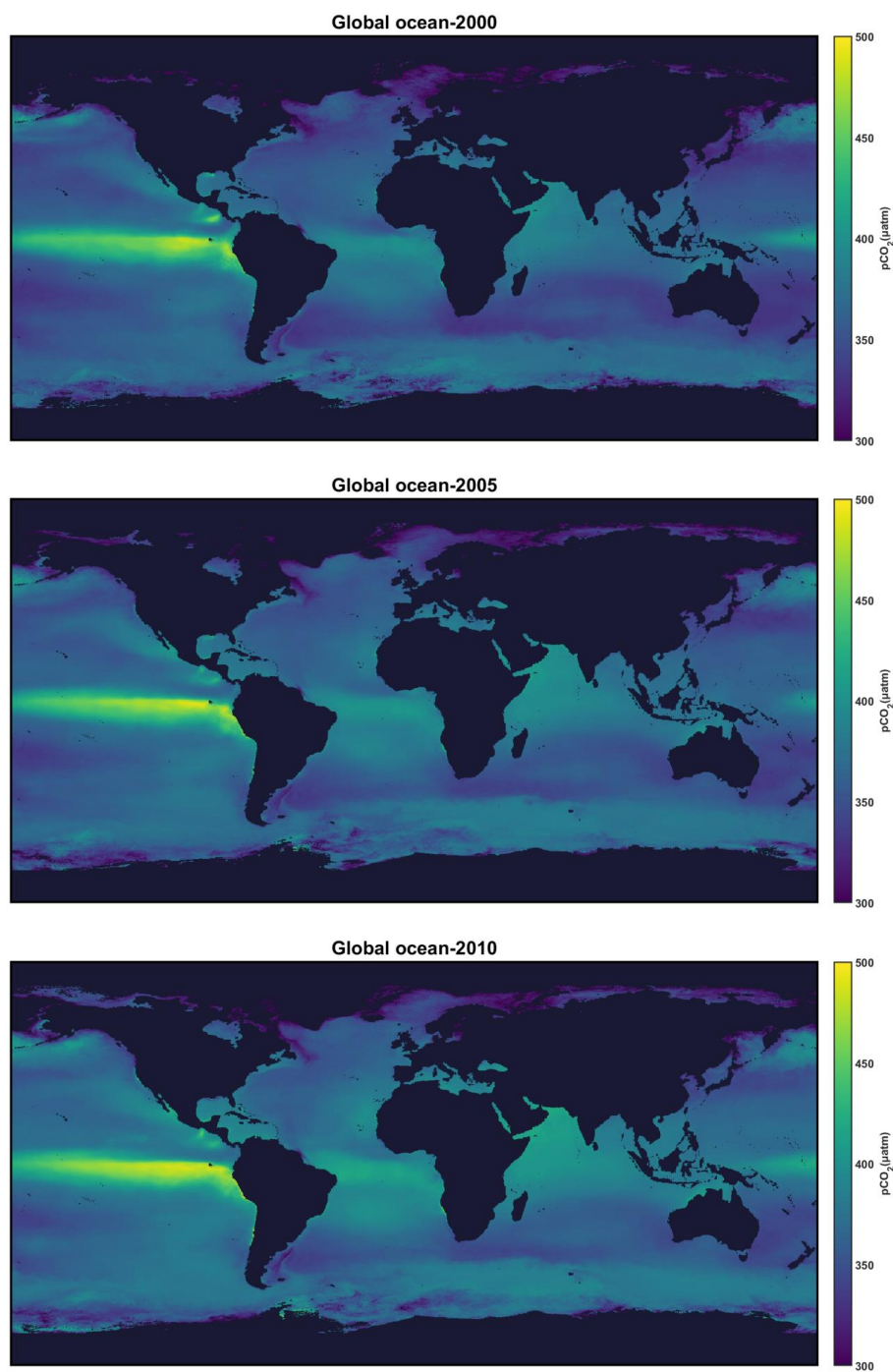
Figure 12. Surface ocean $p\text{CO}_2$ products in the near sea areas



335 **Figure 13. Comparison of reconstruction accuracy in the near sea areas using different scale models, right axis: Normalized probability density of model residuals.**

3.5 Spatiotemporal analysis of surface $p\text{CO}_2$

At the global oceanic scale (Figure 14), the equatorial region experiences strong solar radiation and high temperatures, resulting in relatively low solubility of CO_2 . Additionally, the presence of upwelling brings deep seawater rich in CO_2 to the surface, leading to an increase in surface $p\text{CO}_2$ concentration. Due to the low temperature environment in polar oceans, the solubility of CO_2 in seawater significantly increases. The sea ice coverage and strong wind fields in polar waters promote gas exchange between the atmosphere and the ocean, resulting in relatively low concentrations of $p\text{CO}_2$ on the sea surface. The surface $p\text{CO}_2$ in the Antarctic region is generally higher than that in the Arctic region, because the circulation system transports a large amount of seawater with high surface $p\text{CO}_2$ from low latitudes to high latitudes. At the same time, the melting and formation of sea ice also have an important impact on the distribution of surface $p\text{CO}_2$. Due to the wider coverage of sea ice, the Arctic region is less affected by the North Atlantic warm current, and its surface $p\text{CO}_2$ concentration is lower compared to the Antarctic region. In terms of time, the global ocean surface $p\text{CO}_2$ shows a trend of increasing year by year, which is related to global warming. The rising sea temperature in mid latitude waters leads to a decrease in CO_2 solubility and promotes an increase in surface $p\text{CO}_2$ concentration.



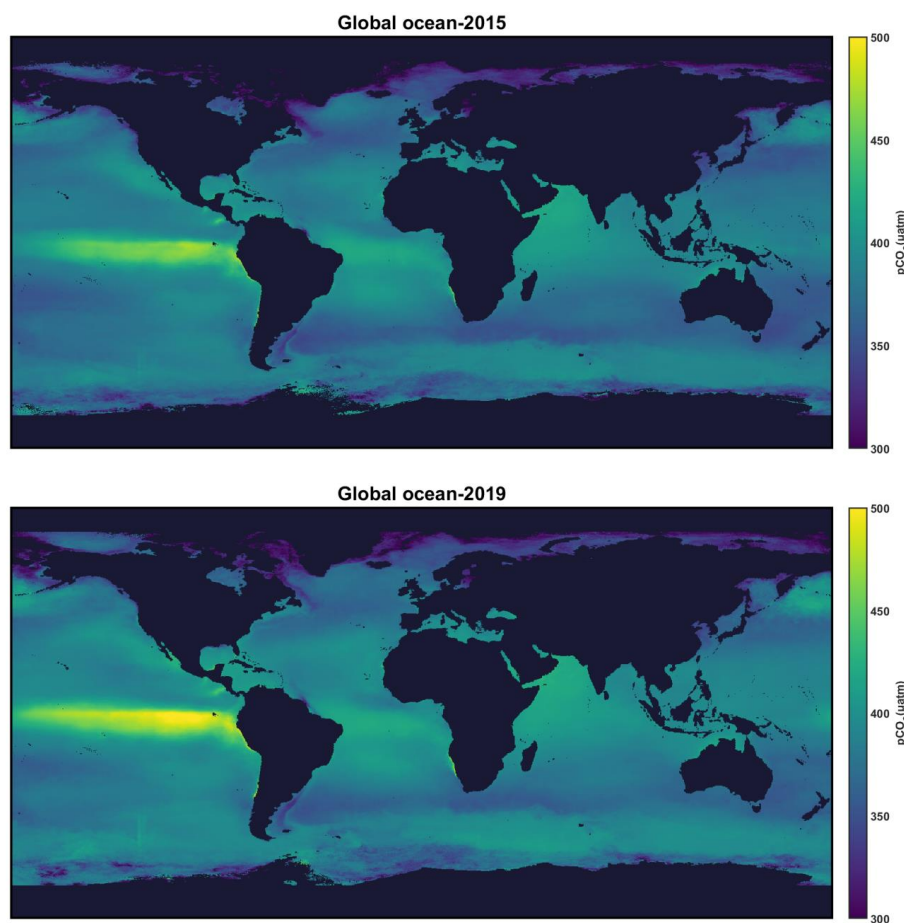
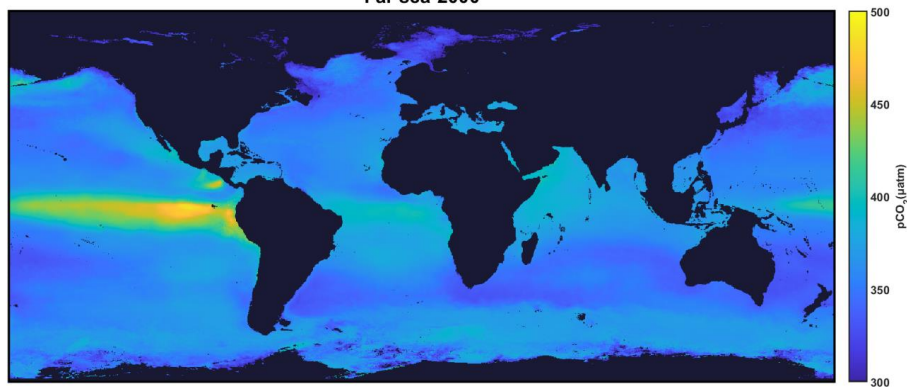


Figure 14. Annual spatiotemporal variations of surface ocean pCO₂ in the global ocean

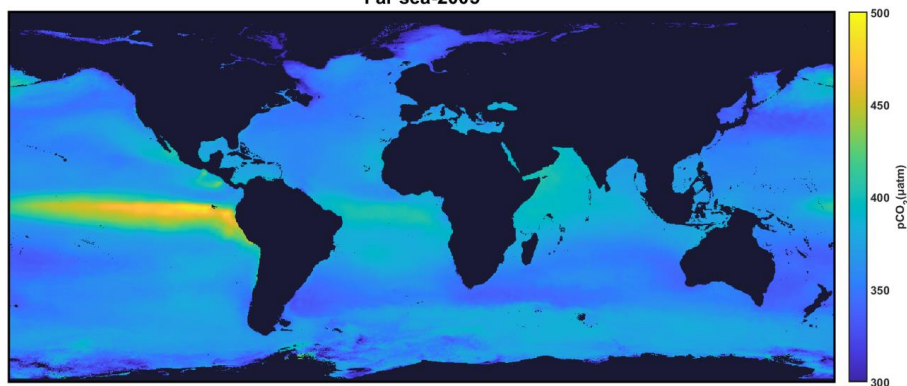
In the far sea areas (Figure 15), the surface pCO₂ is higher in the low latitude areas near the equator, particularly in the eastern equatorial Pacific. Mainly due to the upwelling of seawater in the region, which brings cold water rich in CO₂ from deep layers to the surface of the ocean, resulting in an increase in pCO₂ concentration on the sea surface. In the mid to high latitudes of the far sea region, the surface pCO₂ shows a low characteristic, which is due to the ocean circulation pattern promoting the mixing of surface seawater and deep seawater, resulting in relatively low surface pCO₂ concentration. The low temperature and strong biological pumping effect enhance the absorption of atmospheric CO₂ by the ocean, leading to a low surface pCO₂ concentration. In terms of time, the surface pCO₂ shows a trend of increasing year by year, especially after 2015. This is closely related to global climate change, changes in ocean circulation patterns, and the impact of human activities.



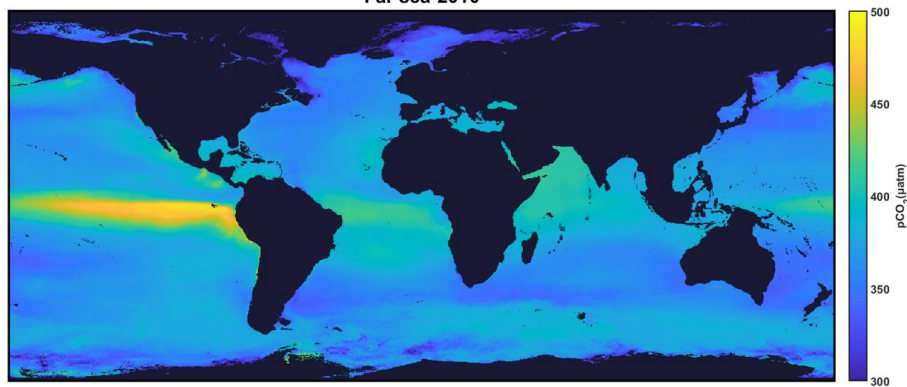
Far sea-2000



Far sea-2005



Far sea-2010



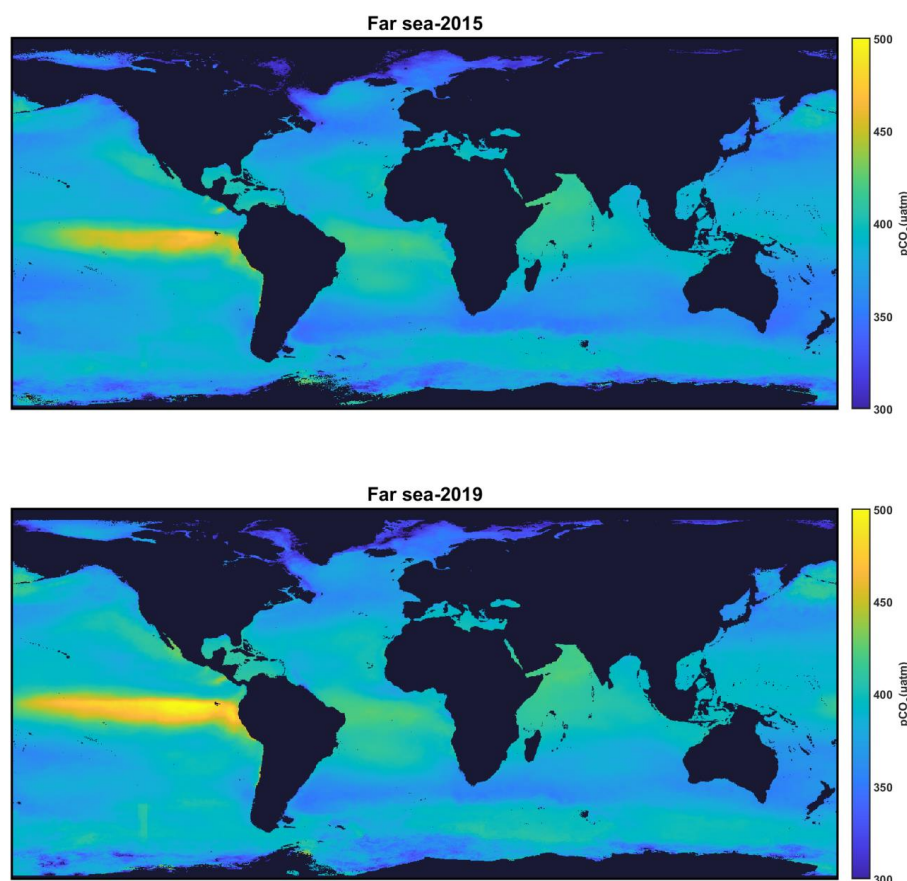
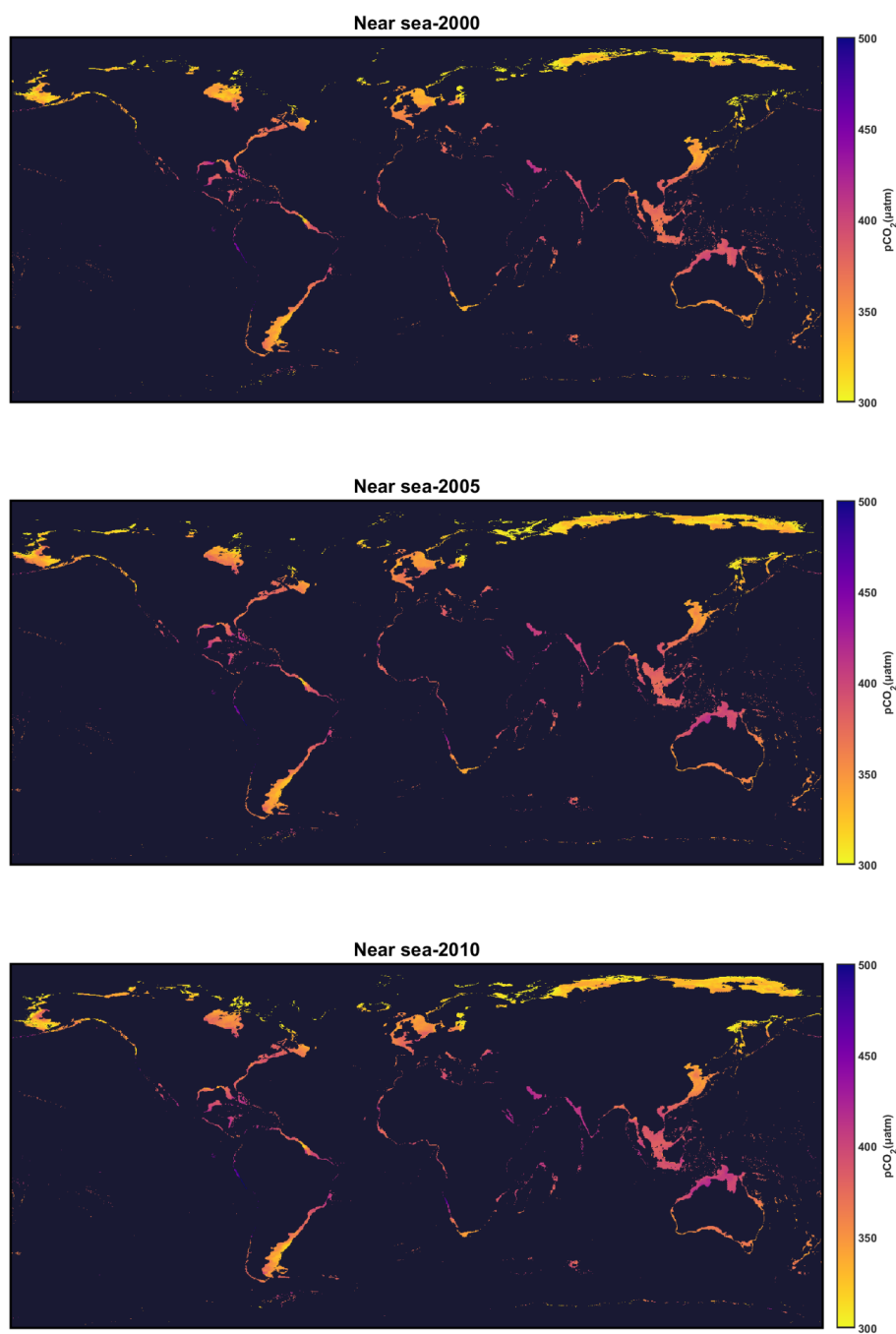


Figure 15. Annual spatiotemporal variations of surface ocean pCO₂ in the far sea areas

The exchange of CO₂ between seawater and atmosphere is frequent, and the surface pCO₂ value is relatively high. In mid to high latitude oceans, low-temperature seawater, polar cold water sinking, and deep seawater upwelling result in relatively low concentrations of pCO₂. The reconstruction results of surface pCO₂ in the near sea area (Figure 16) show that the equatorial region has strong solar radiation, high temperature seawater, and the influence of tropical cyclones and trade winds. The distribution characteristics of surface pCO₂ are significant along the eastern coast of Asia in the mid latitude region of the Northern Hemisphere. The surface pCO₂ in the Yellow Sea and Bohai Sea oceans is significantly lower than that in the coastal areas of eastern North America, which is related to the East Asian monsoon circulation and complex marine ecosystems. The surface pCO₂ in the border waters between Southeast Asia, the Indian Peninsula, North America, and South America is relatively high. Due to the influence of monsoon climate and tropical cyclones, high sea temperatures, as well as marine pollution caused by human activities, have collectively led to an increase in surface pCO₂. Temporally, the surface pCO₂ in near sea areas has been increasing year by year. Due to the increase in temperature in low latitude sea areas, the solubility of CO₂ in seawater decreases, and the upward trend of surface pCO₂ is more pronounced.



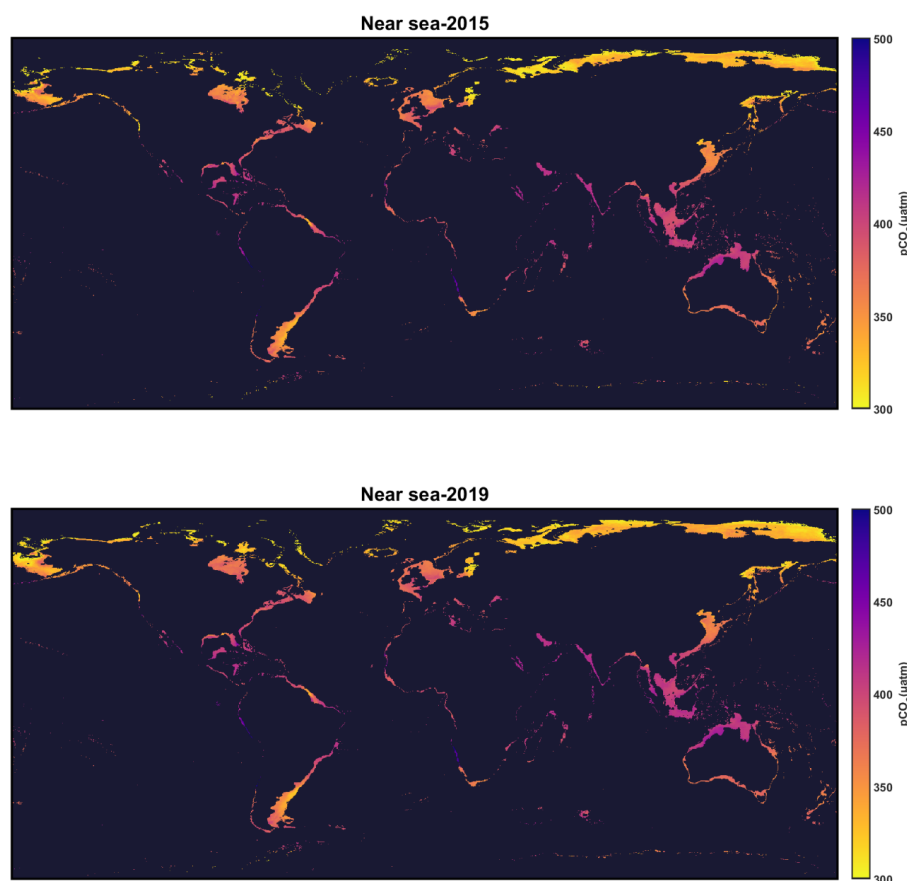


Figure 16. Annual spatiotemporal variations of surface ocean pCO₂ in the near sea areas

This study is based on a multi-scale analysis framework of the global ocean, far sea areas, and near sea areas. Using LDEO measured data combined with multi-source data, multiple machine learning models were used to construct and reconstruct the annual surface pCO₂ distribution of $0.25^\circ \times 0.25^\circ$ from 2000 to 2019, revealing its spatiotemporal variation patterns and driving mechanisms. The research results indicate that the Random Forest (RF) model exhibits optimal performance at different scales and can effectively capture the spatiotemporal distribution characteristics of surface pCO₂. The distribution pattern of surface pCO₂ shows a pattern of "high at the equator and low at the poles" in space, and an increasing trend year by year in time. Different oceans exhibit different characteristics of changes due to the combined effects of natural factors and human activities. The acidity and alkalinity of seawater are the main driving factors for changes in surface pCO₂, and the contributions of other influencing factors vary at different scales.

Although this study has achieved certain results, the complexity of ocean carbon sinks still needs further exploration. Future research can focus on optimizing models, developing hybrid models, and combining advanced algorithms with ocean mechanism models; At the same time, we will strengthen interdisciplinary studies such as oceanography, ecology, and climatology to comprehensively reveal the process of ocean carbon cycling and



390 provide scientific basis for addressing climate change.

Author contribution

Conceptualization, [H.W.]; methodology, [H.W.] and [Y.J.]; software, [X.L.] and [Y.J.]; validation, [W.Z.], [L.C.], and [L.W.]; formal analysis, [Y.J.]; investigation, [W.Z.], [L.W.] and [L.C.]; resources, [X.L.] and [Y.J.]; data curation, [X.L.] and [Y.J.]; writing—original draft preparation, [Y.J.], [Y.W.] and [M.L.]; writing—review and editing, [H.W.] and [Z.L.]; visualization, [X.L.] and [L.C.]; supervision [H.W.]; project administration, [H.W.]; funding acquisition, [H.W.] All authors have read and agreed to the published version of the manuscript.

Competing interests

400 The authors declare that they have no known competing financial interests or personal relationships that could have appeared to influence the work reported in this paper.

Financial support

This research was funded by Key Laboratory of Land Satellite Remote Sensing Application, Ministry of Natural Resources of the People's Republic of China, grant numbers G202211, and the Ministry of Education Industry-University Collaborative Education Project, grant numbers 220504039151258, and the Fundamental Research Funds for the Central Universities, grant numbers 18CX02064A.

Data availability

Data will be made available on request.

410

Reference

- Falkowski, P., Scholes, R. J., Boyle, E., Canadell, J., Canfield, D., Elser, J., . . . Linder, S. J. s. (2000). The global carbon cycle: a test of our knowledge of earth as a system. *290*(5490), 291-296.
- Jain, A. K. (2022). Global carbon budget 2022. *Earth System Science Data*, *14*(11), 4811-4900.
- 415 Qiu, Y., Zhou, J., Khandelwal, M., Yang, H., Yang, P., & Li, C. (2022). Performance evaluation of hybrid WOA-XGBoost, GWO-XGBoost and BO-XGBoost models to predict blast-induced ground vibration. *Engineering with Computers*, *38*(Suppl 5), 4145-4162.
- Chierici M, Signorini S R, Mattsdotter-Björk M, et al. Surface water fCO₂ algorithms for the high-latitude Pacific sector of the Southern Ocean[J]. *Remote Sensing of Environment*, 2012, 119: 184-196.DOI: 10.1016/j.rse.2011.12.020
- 420 Nakaoka S, Telszewski M, Nojiri Y, et al. Estimating temporal and spatial variation of ocean surface pCO₂ in the North Pacific using a self-organizing map neural network technique[J]. *Biogeosciences*, 2013, 10(9):



- 6093-6106.DOI: 10.5194/bg-10-6093-2013
- Landschützer P, Gruber N, Bakker D C E, et al. A neural network-based estimate of the seasonal to inter-annual
425 variability of the Atlantic Ocean carbon sink[J]. Biogeosciences, 2013, 10(11): 7793-7815.DOI:
10.5194/bg-10-7793-2013
- Marrec P, Cariou T, Macé E, et al. Dynamics of air-sea CO₂ fluxes in the North-West European Shelf based on
Voluntary Observing Ship (VOS) and satellite observations[J]. Biogeosciences Discussions, 2015,
12(7).DOI: 10.5194/bgd-12-5641-2015
- 430 Gregor L, Kok S, Monteiro P. Empirical methods for the estimation of Southern Ocean CO₂: support vector and
random forest regression[J]. Biogeosciences, 2017, 14(23): 5551-5569. DOI: 10.5194/bg-14-5551-2017
- Lohrenz S E, Cai W J, Chakraborty S, et al. Satellite estimation of coastal pCO₂ and air-sea flux of carbon
dioxide in the northern Gulf of Mexico[J]. Remote Sensing of Environment, 2018, 207: 71-83.DOI:
10.1016/j.rse.2017.12.039
- 435 Chen S, Hu C, Barnes B B, et al. A machine learning approach to estimate surface ocean pCO₂ from satellite
measurements[J]. Remote Sensing of Environment, 2019, 228: 203-226.DOI: 10.1016/j.rse.2019.04.019
- Fu Z, Hu L, Chen Z, et al. Estimating spatial and temporal variation in ocean surface pCO₂ in the Gulf of
Mexico using remote sensing and machine learning techniques[J]. Science of the Total Environment,
2020, 745: 140965.DOI: 10.1016/j.scitotenv.2020.140965
- 440 Zhang S, Rutgersson A, Philipson P, et al. Remote sensing supported sea surface pCO₂ estimation and variable
analysis in the Baltic Sea[J]. Remote Sensing, 2021, 13(2): 259.DOI: 10.3390/rs13020259
- Wang Y, Li X, Song J, et al. Carbon sinks and variations of pCO₂ in the Southern Ocean from 1998 to 2018
based on a deep learning approach[J]. IEEE Journal of Selected Topics in Applied Earth Observations
and Remote Sensing, 2021, 14: 3495-3503.DOI: 10.1109/JSTARS.2021.3066552
- 445 Landschützer P, Gruber N, Bakker D C E, et al. Recent variability of the global ocean carbon sink[J]. Global
Biogeochemical Cycles, 2014, 28(9): 927-949.DOI: 10.1002/2014GB004853
- Landschützer P, Gruber N, Bakker D C E. Decadal variations and trends of the global ocean carbon sink[J].
Global Biogeochemical Cycles, 2016, 30(10): 1396-1417.DOI: 10.1002/2015GB005359
- Gregor L, Lebehot A D, Kok S, et al. A comparative assessment of the uncertainties of global surface ocean CO₂
450 sub> 2</sub> estimates using a machine-learning ensemble (CSIR-ML6 version 2019a)–have we hit
the wall?[J]. Geoscientific Model Development, 2019, 12(12): 5113-5136.DOI:
10.5194/gmd-12-5113-2019
- Guorong Z, Xuegang L, Baoxiao Q, et al. A general regression neural network approach to reconstruct global
1°× 1° resolution sea surface pCO₂ [J]. Haiyang Xuebao, 2020, 42(10): 70-79. DOI:
455 10.3969/j.issn.0253-4193.2020.10.007
- Zhong G, Li X, Song J, et al. Reconstruction of global surface ocean pCO₂ using region-specific predictors
based on a stepwise FFNN regression algorithm[J]. Biogeosciences, 2022, 19(3): 845-859.DOI:
10.5194/bg-19-845-2022
- Wu H, Wang L, Ling X, et al. Spatiotemporal reconstruction of global ocean surface pCO₂ based on optimized
460 random forest[J]. Science of The Total Environment, 2024, 912: 169209.DOI:
10.1016/j.scitotenv.2023.169209
- Ge W, Patino J, Todisco M, et al. Explaining deep learning models for spoofing and deepfake detection with
SHapley Additive exPlanations[C]//ICASSP 2022-2022 IEEE international conference on acoustics,
speech and signal processing (ICASSP). IEEE, 2022: 6387-6391.DOI:
465 10.1109/ICASSP43922.2022.9747476
- Chau T T T, Gehlen M, Chevallier F. A seamless ensemble-based reconstruction of surface ocean pCO₂ and air–



sea CO₂ fluxes over the global coastal and open oceans[J]. Biogeosciences Discussions, 2021, 2021: 1-30.DOI: 10.5194/bg-19-1087-2022

470 Chau T T T, Chevallier F, Gehlen M. Global analysis of surface ocean CO₂ fugacity and air-sea fluxes with low latency[J]. Geophysical Research Letters, 2024, 51(8): e2023GL106670.DOI: 10.1029/2023GL106670